Transp Porous Med (2010) 83:349–373
DOI 10.1007/s11242-009-9445-7

Calculation of the permeability and apparent permeability of three-dimensional porous media

Rodrigo P. A. Rocha · Manuel E. Cruz

Received: 27 April 2008 / Accepted: 25 June 2009 / Published online: 10 July 2009

Abstract In this study, creeping and inertial incompressible fluid flows through three-dimensional porous media are considered, and an analytical–numerical approach is employed to calculate the associated permeability and apparent permeability. The multiscale homogenization method for periodic structures is applied to the Stokes and Navier–Stokes equations (aided by a control-volume type argument in the latter case), to derive the appropriate cell problems and effective properties. Numerical solutions are then obtained through Galerkin finite-element formulations. The implementations are validated, and results are presented for flows through cubic lattices of cylinders, and through the dendritic zone found at the solid–liquid interface during solidification of metals. For the interdendritic flow problem, a geometric configuration for the periodic cell is built by the approximate matching of experimental and numerical results for the creeping-flow problem; inertial effects are then quantified upon solution of the inertial-flow problem. Finally, the functional behavior of the apparent permeability results is analyzed in the light of existing macroscopic seepage laws. The findings contribute to the (numerical) verification of the validity of such laws.

Keywords Permeability · Apparent permeability · Porous media · Homogenization · Finite-element method

1 Introduction

Fluid flows through porous media take place in many man-made and natural processes, like aerosols filtration, heat transfer in compact heat exchangers, air and water clean-up, resin

---

R. P. A. Rocha
CENPES, Petrobras R&D Center, Cidade Universitária, Rio de Janeiro, RJ 21949-900, Brazil
e-mail: rpenha@petrobras.com.br

M. E. Cruz (✉)
Department of Mechanical Engineering, Politécnica/COPPE, Federal University of Rio de Janeiro,
Caixa Postal 68503, CT, Cidade Universitária, Rio de Janeiro, RJ 21945-970, Brazil
e-mail: manuel@mecanica.coppe.ufrj.br

transfer molding (Ngo and Tamma 2001), and dendritic solidification (Murakami et al. 1983, 1984; Poirier 1987; Brown et al. 2002), to mention but a few examples. When dealing with fluid flows through porous media, the most relevant property of interest is the (tensorial) permeability, which relates the macroscopic pressure drop and the volumetric flow rate as stated by the well-known Darcy's law (Bear 1988; Kaviany 1995). For creeping flows at the pore scale, the permeability depends on the (generally complex) microstructure of the medium only. Owing to the large number of heterogeneities, direct simulation of the fluid flow through the intricate paths of a real porous medium is prohibitive, and analytical results for the permeability are generally restricted to simple geometrical models for the microstructure (e.g., Zick and Homsy 1982).

The phenomenological Darcy's law is verified only when the inertial effects on the flow at the microscale are negligible. However, for many relevant applications, the hypothesis of creeping flow is not verified, and the permeability is seen to depend on both the microstructure of the medium and the Reynolds number of the flow (Edwards et al. 1990; Ghaddar 1995a,b; Kaviany 1995); as a consequence, a nonlinear filtration law rules the fluid seepage at the macroscale. Since the permeability is no longer solely a property of the medium for inertial flows, the name *apparent permeability* is used in the literature (Edwards et al. 1990; Ghaddar 1995a,b). Hereafter, the microstructure-dependent effective property of the porous medium is termed permeability (Bear 1988), while apparent permeability will denote, the effective property that depends on both the medium microstructure and flow Reynolds number (Lucas et al. 2007).

In this study, an analytical–numerical approach is employed to predict numerical values for the permeability and apparent permeability of three-dimensional porous media, whose microstructures are known a priori (Rocha 2007). The approach is based on a homogenization method for periodic structures (Hornung 1997; Auriault 2001), a control-volume type argument for the inertial-flow case (Ghaddar 1995a,b), and the finite-element method (Reddy and Gartling 2001). The main contributions of the present study are twofold. First, a rational, physically sound, and accurate procedure is provided, to predict the apparent permeability of a three-dimensional porous medium, whose microstructure is given explicitly, and has been previously validated in the creeping-flow regime. This methodical calculation route appears new in the literature. Second, the examination of, and findings about, the functional behavior of the apparent permeability results for the 3-D periodic microstructures of this study contribute to the numerical verification of the validity of existing porous media macroscopic seepage laws (Firdaouss et al. 1997; Skjetne and Auriault 1999; Chen et al. 2001; Fourar et al. 2004; Lucas et al. 2007).

For completeness of the article, the homogenization equations are briefly derived in Sect. 2, from both the Stokes and Navier–Stokes equations at the pore scale. In Sect. 3, the appropriate cell problems are stated in weak form, and the finite-element solution procedure, based on a classical Galerkin formulation, is outlined. In Sect. 4, the geometrical configurations of interest for the solution of the cell problems are presented; among them, the three-dimensional cubic lattices of cylinders of Higdon and Ford (1996), and a microstructure typical of the so-called "mushy zone", for simulating the flow through the interdendritic region during solidification of alloys, are considered. In Sect. 5, (i) the implementations are validated for both creeping and inertial flows against results available in the literature, (ii) new results for inertial flow through the cubic lattices of cylinders are obtained, (iii) the dendritic-microstructure geometrical configuration for the periodic cell is tested against experimental results for creeping flow, (iv) inertial effects are quantified for flow parallel to the primary dendrite arms of the latter microstructure, and (v) an examination of the functional behavior of the apparent permeability results in the light of existing macroscopic filtration laws is effected. Finally, in Sect. 6, the conclusions of the present study are stated.

2 Homogenization

Let $\Omega \subset R^3$ be a bounded domain with boundary $\partial\Omega$; $\Omega = \Omega_f \cup \Omega_s$, where Ω_f is a connected continuous fluid phase, and Ω_s is the dispersed solid phase. The interface between the fluid and solid phases is denoted by Γ. The fluid is assumed Newtonian and incompressible, with density ρ and dynamic viscosity μ. The solid phase consists of a fixed bed of fibers randomly distributed and oriented in space. A pressure gradient $(\Delta P/L)\mathbf{e}_m$ is imposed over the macroscale L in the x_m^*-direction; $\mathbf{e}_m$ is the unit vector parallel to the x_m^*-axis. The multiscale medium is assumed periodic at the microscale $l \ll L$ in all coordinate directions, so that the small parameter $\epsilon \equiv l/L \ll 1$, and the multiscale homogenization method (Auriault 2001) can be applied.

2.1 Creeping Flow

When inertial effects are negligible, Stokes equations govern the fluid motion,

$$\frac{\partial p}{\partial x_i} = \frac{\mu V}{L\,\Delta P}\frac{\partial^2 u_i}{\partial x_j \partial x_j} \quad \text{in } \Omega_f\,, \quad i = 1, 2, 3, \tag{1}$$

$$\frac{\partial u_i}{\partial x_i} = 0 \quad \text{in } \Omega_f\,, \tag{2}$$

and the no-slip condition applies

$$u_i = 0 \quad \text{on } \Gamma\,. \tag{3}$$

In the non-dimensional Eqs. 1–3, summation over repeated indices is implied,

$$\mathbf{x} \equiv \frac{\mathbf{x}^*}{L}, \quad \mathbf{u} \equiv \frac{\mathbf{u}^*}{V}, \quad p \equiv \frac{p^*}{\Delta P}, \tag{4}$$

$\mathbf{x}^* = (x_1^*, x_2^*, x_3^*) \in R^3$ is the spatial coordinate, $\mathbf{u}^* = (u_1^*, u_2^*, u_3^*)$ is the velocity field, V is a characteristic velocity, and p^* is the pressure field. Body forces are neglected. The *homogenization condition* to ensure that the velocity has a non-trivial limit when $\epsilon \to 0$ requires $\mu V/L\,\Delta P = O(\epsilon^2)$ (Hornung 1997; Auriault 2001).

The medium can be partitioned into $N = O(\epsilon^3)$ periodic cells $Q_n^\epsilon, n = 1, 2, \ldots, N$, of characteristic length l, and $\Omega = \bigcup_{n=1}^N Q_n^\epsilon$; microscopically, each cell Q_n^ϵ is mapped onto a reference periodic cell Q of characteristic length $l_0 = O(l)$, such that the geometry of Q defines the microstructure of the periodic medium completely. Separation of length scales thus permits one to write both velocity and pressure as

$$u_i(\mathbf{x}) = u_i(\mathbf{x}, \mathbf{y}) = \sum_{k=0}^{\infty} \epsilon^k u_i^{(k)}(\mathbf{x}, \mathbf{y}), \quad p(\mathbf{x}) = p(\mathbf{x}, \mathbf{y}) = \sum_{k=0}^{\infty} \epsilon^k p^{(k)}(\mathbf{x}, \mathbf{y}), \tag{5}$$

where $\mathbf{x}$ and $\mathbf{y} = \mathbf{x}/\epsilon$ are the macroscopic (slow) and microscopic (fast) coordinates, respectively. Inserting 5 into 1–3, and collecting the terms of order ϵ^{-1} and ϵ^0, one concludes that (Hornung 1997)

$$\frac{\partial p^{(0)}}{\partial x_i} = \frac{\partial p^{(0)}}{\partial x_m} = \mathbf{e}_m \tag{6}$$

and

$$u_i^{(0)}(\mathbf{x}, \mathbf{y}) = -K_{im} \frac{\partial p^{(0)}}{\partial x_m}, \tag{7}$$

$m \in \{1, 2, 3\}$. Writing Q_f and ∂Q_f for the fluid part of the periodic cell Q and of its boundary ∂Q, respectively, and Γ_Q for the solid–liquid interface in Q, the fields $K_{im}(\mathbf{y})$ and $\Pi_m(\mathbf{y})$ are periodic over ∂Q_f, and satisfy

$$\frac{\partial^2 K_{im}}{\partial y_j \partial y_j} = \frac{\partial \Pi_m}{\partial y_i} - \delta_{im} \quad \text{in } Q_f, \quad i = 1, 2, 3, \tag{8}$$

$$\frac{\partial K_{im}}{\partial y_i} = 0 \quad \text{in } Q_f, \tag{9}$$

$$K_{im} = 0 \quad \text{on } \Gamma_Q. \tag{10}$$

In order to ensure uniqueness, the condition $\Pi_m(\tilde{\mathbf{y}}) = 0$ is further imposed at an arbitrary point $\tilde{\mathbf{y}}$ of Q_f.

Darcy's law (Bear 1988; Kaviany 1995) relates the dimensional superficial velocity $\mathbf{q}$ and the dimensional pressure gradient $\mathbf{G}$ for the creeping flow of a viscous incompressible Newtonian fluid through a porous medium by the expression

$$q_i = -\frac{k_{im}^* G_m}{\mu}, \tag{11}$$

where $\mathbf{k}^* = k_{im}^*$ is the permeability tensor, strictly a property of the medium. Averaging Eq. 7 over the cell domain, one obtains the following non-dimensional form for Darcy's law,

$$\frac{1}{|Q|} \int_Q u_i^{(0)} \, d\mathbf{y} = -\left(\frac{1}{|Q|} \int_Q K_{im} \, d\mathbf{y} \right) \frac{\partial p^{(0)}}{\partial x_m}, \tag{12}$$

where $|Q| = O(l^3)$ is the cell volume. Inspecting Eqs. 11 and 12, the following expression for the non-dimensional permeability tensor is derived:

$$k_{im} = \frac{k_{im}^*}{l^2} = \frac{1}{|Q|} \int_Q K_{im} \, d\mathbf{y}. \tag{13}$$

Thus, solution of the periodic cell problem 8–10 for a given medium microstructure, defined by the cell Q, leads to the permeability tensor given by the expression 13.

2.2 Inertial Flow

Homogenization theory has already been applied to inertial flows. Mei and Auriault (1991) consider weak inertial effects only, while Marušic-Paloka and Mikelic (2000) and Chen et al. (2001) assume that the inertial terms have the same order of magnitude as the viscous and pressure terms; here, the latter approach is followed. Although Marušic-Paloka and Mikelic (2000) and Chen et al. (2001) present rigorous homogenization procedures to obtain the periodic cell and homogenized problems, they do not consider the unsteady effects, which are relevant for moderate Reynolds numbers (Ghaddar 1995a,b). G. Allaire (Hornung 1997, chap. 3) states, without proof, that convective and unsteady effects combined can indeed be treated by the homogenization method.

In order to consider both convective and unsteady effects, it thus seems appropriate to adopt a widely accepted, physically plausible model based on a control-volume type argument (Ghaddar 1995a,b): the contribution of the external boundary conditions to the microscopic flow occurs solely via the macroscopic pressure gradient, as shown for the creeping-flow cell problem. Based on 8–10, a periodic cell Navier–Stokes problem for the unsteady inertial incompressible flow may then be inferred: given Re', find the (nondimensional) fields $K_{im}(\mathbf{y})$ and $\Pi_m(\mathbf{y})$ that are periodic over ∂Q_f, and that satisfy (with $m \in \{1, 2, 3\}$ and no sum over m)

$$\frac{\partial K_{im}}{\partial t} + K_{jm}\frac{\partial K_{im}}{\partial y_j} - \frac{1}{Re'}\frac{\partial^2 K_{im}}{\partial y_j \partial y_j} + \frac{\partial \Pi_m}{\partial y_i} = \delta_{im} \quad \text{in } Q_f, \quad i = 1, 2, 3, \tag{14}$$

$$\frac{\partial K_{im}}{\partial y_i} = 0 \quad \text{in } Q_f, \tag{15}$$

$$K_{im} = 0 \quad \text{on } \Gamma_Q, \tag{16}$$

and the uniqueness condition $\Pi_m(\tilde{\mathbf{y}}) = 0$. The Reynolds number Re' in Eq. 14 is defined as $Re' = \frac{\rho V d}{\mu}$, where d is the cylinder diameter and $V = \sqrt{\frac{\Delta P d}{\rho L}}$.

When inertial effects are not negligible, the pressure gradient and the superficial velocity are not related linearly, and Darcy's law is no longer appropriate. Nevertheless, the linear representation given by Eq. 11 (or by Eq. 12) is still convenient. In order to account for the non-linear effects, the tensor $\mathbf{k}^{a*}$ is made to depend not only on the microstructure but also on the Reynolds number Re'; $\mathbf{k}^{a*}$ is known as the *apparent permeability* (Edwards et al. 1990). As an unsteady flow is considered here, the macroscopic (or effective) property—the apparent permeability—must be time-averaged. It can be shown that the non-dimensional apparent permeability tensor is given by (Ghaddar 1995a,b)

$$k^a_{im} = \frac{k^{a*}_{im}}{l^2} = \frac{1}{T\,|Q|\,Re'}\int_0^T \int_Q K_{im}(\mathbf{y}, t)\,\mathrm{d}\mathbf{y}\,\mathrm{d}t, \tag{17}$$

where $\mathbf{K}(\mathbf{y}, t)$ is the solution of the cell problem 14–16, and T is the characteristic time period of the unsteady flow. In general, due to the complex microstructures of real porous media, analytical solutions of the cell problem are impractical, and a numerical approach is required.

3 Finite-Element Formulations

Finite elements (Reddy and Gartling 2001) are well-suited for the generally complex three-dimensional geometries of typical porous media. In this section, Galerkin finite-element formulations are presented for solving the cell problems for both creeping (Eqs. 8–10) and inertial flows (Eqs. 14–16), using unstructured tetrahedral meshes.

3.1 Domain Discretization

The first step to a successful finite-element solution is an appropriate discretization of the domain. Here, the fluid domain Q_f is discretized through an unstructured conforming periodic mesh consisting of N_e tetrahedral elements, constructed by the resourceful third-party software NETGEN 4.0 (Schöberl 2001).

Since the creeping-flow problem does not require large CPU times, fine uniform meshes are used throughout the corresponding domains. On the other hand, the inertial-flow problem does require a substantial amount of CPU time. Therefore, a selective mesh refinement procedure is needed, such that a first solution of the cell problem on a coarse uniform mesh is found. A new non-uniform mesh is then constructed with finer elements, where the gradients of K_{pm} are higher. Defining $g(\mathbf{y}) \equiv \partial K_{pm}/\partial y_p$, the characteristic size h of the edge of a tetrahedron is then given by

$$\begin{aligned} h(\mathbf{y}) &= \frac{h_0\, g_{\text{ref}}}{\zeta\; g(\mathbf{y})} \quad \text{where} \quad g(\mathbf{y}) > g_{\text{ref}}\ , \quad \text{and} \\ h(\mathbf{y}) &= h_0 \quad \text{elsewhere.} \end{aligned} \tag{18}$$

In Eq. 18, h_0 is the nominal mesh size, ζ is a global refinement parameter, and g_{ref} is a reference value for the gradient, which determines, where the mesh will be refined. Here, $g_{\text{ref}} = a_1\, \bar{g}, a_1 \in R$, where $\bar{g}$ is the average of $g(\mathbf{y})$ over the domain, and a_1 is typically chosen to be (close to) 1.

3.2 Problems Discretization

3.2.1 Creeping Flow

Let $L(Q)$ be the space of scalar periodic functions that are square-integrable in Q, and $H(Q)$ the space of scalar periodic functions whose derivatives with respect to y_i, $i = 1, 2, 3$, belong to $L(Q)$. The weak form of the cell problem 8–10 is written as (Ghaddar 1995a,b): given $m \in \{1, 2, 3\}$, find $(K_{1m}, K_{2m}, K_{3m}, \Pi_m) \in ([H(Q)]^3, L(Q))$ such that, for all $(v_1, v_2, v_3, w) \in ([H(Q)]^3, L(Q))$,

$$\int_Q \frac{\partial v_i}{\partial y_j}\frac{\partial K_{im}}{\partial y_j}\, \mathbf{dy} - \int_Q \Pi_m \frac{\partial v_i}{\partial y_i}\, \mathbf{dy} = \int_Q v_m\, \mathbf{dy}\ , \tag{19}$$

$$\int_Q w \frac{\partial K_{im}}{\partial y_i}\, \mathbf{dy} = 0\, , \tag{20}$$

subject to the no-slip boundary condition 10, and the uniqueness condition $\Pi_m(\tilde{\mathbf{y}}) = 0$.

In order to satisfy the Ladyzhenskaya–Babuska–Brezzi (LBB) consistency condition for incompressible flows (Reddy and Gartling 2001), Taylor–Hood isoparametric 10-node tetrahedra are used for the finite-element discretization of Eqs. 19–20. Velocity components and the geometry are thus interpolated quadratically, while the pressure is interpolated linearly. The discrete global velocity and pressure fields can be written as (superscript h denotes discrete quantities):

$$K^h_{im}(\mathbf{y}) = \sum_{a=1}^{N_U} U^i_a \Psi_a(\mathbf{y}) \quad \text{and} \quad \Pi^h_m(\mathbf{y}) = \sum_{a=1}^{N_P} P_a \Phi_a(\mathbf{y}). \tag{21}$$

In Eq. 21, U^i_a is the unknown value of the i-component of the velocity field $\mathbf{K}^h_m$ at node a, $a = 1, \ldots, N_{\text{dof,v}}$; $N_{\text{dof,v}}$ is the number of unknown values (degrees-of-freedom) of K^h_{im}. Analogously, P_a is the unknown value of the pressure field Π^h_m at node a, $a = 1, \ldots, N_{\text{dof,p}}$; $N_{\text{dof,p}}$ is the number of unknown values of Π^h_m. The quadratic and linear finite-element interpolation functions at node a of a 10-node tetrahedron are $\Psi_a(\mathbf{y})$ and $\Phi_a(\mathbf{y})$, respectively. In a Galerkin formulation, the weighting functions are approximated by the interpolation functions themselves (Reddy and Gartling 2001), such that

$$v^h_i(\mathbf{y}) = \Psi_a(\mathbf{y}) \quad \text{and} \quad w^h(\mathbf{y}) = \Phi_a(\mathbf{y}). \tag{22}$$

Locally, the velocity $\mathbf{K}_m$ and the pressure are calculated, respectively, at the ten (corner and midside) nodes and at the four corner nodes of every quadratic tetrahedron.

The discrete weak form of the cell problem 19–20 can now be written: given $m \in \{1, 2, 3\}$, find the periodic fields $(K_{1m}^h, K_{2m}^h, K_{3m}^h, \Pi_m^h) \in ([H_h(Q)]^3, L_h(Q))$ such that, for all $(v_1^h, v_2^h, v_3^h, w^h) \in ([H_h(Q)]^3, L_h(Q))$,

$$\int_{Q_h} \frac{\partial v_i^h}{\partial y_j} \frac{\partial K_{im}^h}{\partial y_j} \, \mathbf{dy} - \int_{Q_h} \Pi_m^h \frac{\partial v_i^h}{\partial y_i} \, \mathbf{dy} = \int_{Q_h} v_m^h \, \mathbf{dy}, \tag{23}$$

$$\int_{Q_h} w^h \frac{\partial K_{im}^h}{\partial y_i} \, \mathbf{dy} = 0, \tag{24}$$

$$K_{im}^h = 0 \quad \text{on } \Gamma_Q^h, \tag{25}$$

subject to $\Pi_m^h(\tilde{\mathbf{y}}) = 0$. In Eqs. 23–25, Q_h is the finite-element mesh, i.e., the union of all tetrahedra $\tau_e, \; e = 1, \ldots, N_e$. The function spaces for velocity and pressure are $L_h(Q) = L(Q) \cap Y_1(\tau_e)$ and $H_h(Q) = H(Q) \cap Y_2(\tau_e)$, respectively, where $Y_p(\tau_e)$ is the space of all polynomials of degree p defined over element τ_e. Substituting Eqs. 21–22 into the discrete cell problem 23–25 and performing numerical integration, one obtains the following system of linear algebraic equations (Ghaddar 1995a,b):

$$[A]\{U^i\} - [D_i]^T\{P\} = [M]\{f_i\}, \quad i = 1, 2, 3, \tag{26}$$

$$[D_i]\{U^i\} = \{0\}, \tag{27}$$

where $[A]$ is the symmetric discrete Laplacian operator, $[D_i]$ is the discrete divergence operator, $[M]$ is the mass matrix, vector $\{f_i\}$ represents the non-dimensional external pressure gradient, and vectors $\{U^i\}$ and $\{P\}$ comprise, respectively, the i-component of the velocity and pressure nodal unknowns (see Eq. 21). Here, integration is performed with a 35-point Gaussian quadrature formula. In order to satisfy Eq. 25, null velocity is imposed at every node on the interface Γ_Q^h; these known nodal velocity values are not part of the unknown vector $\{U^i\}$.

3.2.2 Inertial Flow

The discretization procedure for the cell problem of the inertial-flow case is analogous to that of the creeping-flow case. The weak form of problem 14–15 is written as (Ghaddar 1995a,b): given $m \in \{1, 2, 3\}$ and Re', find $(K_{1m}, K_{2m}, K_{3m}, \Pi_m) \in ([H(Q)]^3, L(Q))$ such that, for all $(v_1, v_2, v_3, w) \in ([H(Q)]^3, L(Q))$,

$$\begin{aligned} &\int_Q v_i \frac{\partial K_{im}}{\partial t} \, \mathbf{dy} + \int_Q v_i K_{jm} \frac{\partial K_{im}}{\partial y_j} \, \mathbf{dy} + \frac{1}{Re'} \int_Q \frac{\partial v_i}{\partial y_j} \frac{\partial K_{im}}{\partial y_j} \, \mathbf{dy} \\ &- \int_Q \Pi_m \frac{\partial v_i}{\partial y_i} \, \mathbf{dy} = \int_Q v_m \, \mathbf{dy}, \end{aligned} \tag{28}$$

$$\int_Q w \frac{\partial K_{im}}{\partial y_i} \, \mathbf{dy} = 0, \tag{29}$$

subject to the no-slip boundary condition 16, and the uniqueness condition $\Pi_m(\tilde{\mathbf{y}}) = 0$.

Considering the same interpolation rules adopted in the creeping-flow problem (see Eqs. 21–22) and the discrete spaces $L_h(Q)$ and $H_h(Q)$, the discrete weak form of the cell problem 28–29 can be stated as: given $m \in \{1, 2, 3\}$ and Re', find the periodic fields

$(K_{1m}^h, K_{2m}^h, K_{3m}^h, \Pi_m^h) \in ([H_h(Q)]^3, L_h(Q))$ such that, for all $(v_1^h, v_2^h, v_3^h, w^h) \in ([H_h(Q)]^3, L_h(Q))$,

$$\int_{Q_h} v_i^h \frac{\partial K_{im}^h}{\partial t} \, \mathbf{dy} + \int_{Q_h} v_i^h K_{jm}^h \frac{\partial K_{im}^h}{\partial y_j} \, \mathbf{dy} + \frac{1}{Re'} \int_{Q_h} \frac{\partial v_i^h}{\partial y_j} \frac{\partial K_{im}^h}{\partial y_j} \, \mathbf{dy}$$
$$- \int_{Q_h} \Pi_m^h \frac{\partial v_i^h}{\partial y_i} \, \mathbf{dy} = \int_{Q_h} v_m^h \, \mathbf{dy}, \tag{30}$$

$$\int_{Q_h} w^h \frac{\partial K_{im}^h}{\partial y_i} \, \mathbf{dy} = 0, \tag{31}$$

$$K_{im}^h = 0 \quad \text{on } \Gamma_Q^h, \tag{32}$$

subject to $\Pi_m^h(\tilde{\mathbf{y}}) = 0$. Substituting Eqs. 21–22 into 30–32, and performing numerical integration, one obtains the following system of linear algebraic equations (Ghaddar 1995a,b):

$$[M]\frac{\mathrm{d}}{\mathrm{d}t}\{U^i\} + [C]\{U^i\} = -\frac{1}{Re'}[A]\{U^i\} + [D_i]^T\{P\} + [M]\{f_i\}, \quad i = 1, 2, 3, \tag{33}$$

$$[D_i]\{U^i\} = \{0\}, \tag{34}$$

where $[C]$ is the *non-symmetric non-linear* convective operator, which depends on the solution $\{U^i\}$. As mentioned in Sect. 3.2.1, integration is performed with a 35-point Gaussian quadrature formula.

For a time-stepping solution procedure, the viscous term is integrated through an implicit backward scheme, and the nonlinear term is treated explicitly by the 3rd-order Adams–Bashforth scheme, leading to the following *symmetric linear* system of algebraic equations (Ghaddar 1995a,b):

$$\left(\frac{1}{Re'}[A] + \frac{1}{\Delta t_n}[M]\right)\{U^i\}_{n+1} - [D_i]^T\{P\}_{n+1}$$
$$= \frac{1}{\Delta t_n}[M]\{U^i\}_n - \sum_{p=0}^{2} \alpha_p [C]_{n-p}\{U^i\}_{n-p} + [M]\{f_i\}, \quad i = 1, 2, 3, \tag{35}$$

$$[D_i]\{U^i\} = \{0\}, \tag{36}$$

where the subscript n refers to the nth iteration, Δt_n is the time step, and α_0, α_1, and α_2 are coefficients, which depend on the last three time steps:

$$\begin{aligned}
\alpha_0 &= \frac{12\Delta t_{n-1}(\Delta t_{n-1} + \Delta t_{n-2}) + 6\Delta t_n(2\Delta t_{n-1} + \Delta t_{n-2}) + 4\Delta t_n^2}{12\Delta t_{n-1}(\Delta t_{n-1} + \Delta t_{n-2})}, \\
\alpha_1 &= -\frac{6\Delta t_n(\Delta t_{n-1} + \Delta t_{n-2}) + 4\Delta t_n^2}{12\Delta t_{n-1}\Delta t_{n-2}}, \\
\alpha_2 &= \frac{6\Delta t_n \Delta t_{n-1} + 4\Delta t_n^2}{12\Delta t_{n-2}(\Delta t_{n-1} + \Delta t_{n-2})}.
\end{aligned} \tag{37}$$

The notation $[C]_{n-p}$ indicates that the matrix $[C]$ is evaluated with the solution obtained at iteration $n - p$, namely, $\{U^i\}_{n-p}$.

3.3 Solution of the Algebraic Systems

In this section, the iterative solution procedures to solve the creeping-flow system 26–27 and the inertial-flow system 35–36 are summarized. As in Ghaddar (1995a,b), the iterative procedures are based on the conjugate gradient method (Shewchuk 1994) and on the element-by-element evaluation technique, by means of which the global matrices need not be assembled. The stopping criterion for an iterative solve is based on the norm of the residual, which has to reach a sufficiently small value; ultimately, the solves yield the significant digits presented in Sect. 5.

3.3.1 Creeping Flow

The system of algebraic equations 26–27 is solved through the Uzawa saddle-decoupling algorithm (Maday et al. 1993; Ghaddar 1995a,b): multiplying Eq. 26 on the left by $[D_i][A]^{-1}$, and using 27, leads to

$$[S]\{P\} = -[D_i][A]^{-1}[M]\{f_i\}, \tag{38}$$

where $[S] \equiv [D_i][A]^{-1}[D_i]^T$ is a symmetric positive-definite operator; from 26,

$$[A]\{U^i\} = [D_i]^T\{P\} + [M]\{f_i\}, \quad i = 1, 2, 3. \tag{39}$$

A nested conjugate gradient procedure is adopted to solve Eq. 38 for $\{P\}$. Defining $\{Z_i\} \equiv [A]^{-1}[M]\{f_i\}$, a conjugate gradient iteration is used to find $\{Z_i\}$ from $[A]\{Z_i\} = [M]\{f_i\}$. The right-hand-side of Eq. 38 is then easily obtained,

$$-[D_i][A]^{-1}[M]\{f_i\} = -[D_i]\{Z_i\}. \tag{40}$$

The velocity solutions $\{U^i\}$ are found by solving Eq. 39 via a simple conjugate gradient iteration for each i, $i = 1, 2, 3$.

3.3.2 Inertial Flow

In order to solve the indefinite system 35–36, an operator splitting method is employed (Maday et al. 1990; Ghaddar 1995a,b), yielding the system:

$$\begin{aligned}
[H]\{\tilde{U}^i\}_{n+1} &= [D_i]^T\{P\}_n + \frac{1}{\Delta t_n}[M]\{U^i\}_n - \sum_{p=0}^{2} \alpha_p [C]_{n-p}\{U^i\}_{n-p} + [M]\{f_i\}, \\
i &= 1, 2, 3, && (41)\\
[E]\{P\}_{n+1} &= [E]\{P\}_n - \frac{1}{\Delta t_n}[D_i]\{\tilde{U}^i\}_{n+1}, && (42)\\
\{U^i\}_{n+1} &= \{\tilde{U}^i\}_{n+1} + \Delta t_n [M]^{-1}[D_i]^T(\{P\}_{n+1} - \{P\}_n), && (43)
\end{aligned}$$

where $\{\tilde{U}^i\}$ is an intermediate (velocity) solution, and $[H]$ and $[E]$ are the Helmholtz and Poisson operators, respectively, defined as

$$[H] \equiv \frac{1}{Re'}[A] + \frac{1}{\Delta t_n}[M] \quad \text{and} \quad [E] \equiv [D_i][M]^{-1}[D_i]^T. \tag{44}$$

The mass matrix $[M]$ is then replaced by the diagonal lumped mass matrix $[M_L]$, defined *locally* in the tetrahedral element τ_e as (no sum over j)

$$[M_L]_{jj}^{\tau_e} \equiv [M]_{jj}^{\tau_e} \frac{|\tau_e|}{\mathrm{tr}[M]^{\tau_e}}, \tag{45}$$

where $|\tau_e|$ is the volume of tetrahedron τ_e. This matrix replacement eliminates the need for a nested conjugate gradient loop to solve Eq. 43, reducing computational time, and its associated error vanishes completely at steady-state.

For the time-stepping procedure, the time step for iteration $n+1$ is calculated based on the Courant condition for iteration n. For every edge h_k $(k = 1, 2, \dots, 6)$ of every tetrahedron τ_e $(e = 1, 2, \dots, N_e)$, a Courant number is defined as

$$Cr = u\Delta t_n/(h_k/2), \tag{46}$$

where u is the projection of the velocity vector on the edge h_k, and $(h_k/2)$ is used as the reference mesh size due to the quadratic interpolation. For the finite-difference scheme, described in Sect. 3.2.2, a stable solution is guaranteed when $Cr_{\max} < 0.723$ over the mesh (Ghaddar 1995a). If, this criterion is not observed, the entire calculation carried out at iteration n is abandoned, and a new time step Δt_n, calculated with $Cr = 0.5$, is considered:

$$\Delta t_n = 0.5\frac{h_k}{2u}. \tag{47}$$

The choice $Cr = 0.5$ will provide stable solutions for the range of Reynolds numbers considered in the present study. Thus, for iteration $n+1$, if the stability criterion $(Cr_{\max} < 0.723)$ is verified, the same time step is used, provided it is larger than the one given in Eq. 47; otherwise, the value calculated in Eq. 47 is used.

3.4 Calculation of the Permeabilities

3.4.1 Creeping Flow

Once system 38–39 is solved, the permeability tensor $\mathbf{k}_h$ can be calculated. In this article, only the most relevant permeability entries k_{mm} are considered, so that, choosing $m = 1$, the expression for the numerical (scalar) permeability is

$$k_h \equiv k_{h,11} = \frac{1}{|Q_h|}\int_{Q_h} K_{11}^h \, \mathrm{d}\mathbf{y}. \tag{48}$$

Alternative expressions to evaluate k_h are (sum over i):

$$k_h = \frac{1}{|Q_h|}\{U^i\}^T[A]\{U^i\} = \frac{1}{|Q_h|}\{1\}^T[M]\{U^1\}. \tag{49}$$

Equation 49 serves as a useful check for the implementation, in that it should lead to the same value for k_h as Eq. 48.

3.4.2 Inertial Flow

Analogously to the creeping-flow permeability calculation, once system 41–43 is solved, the numerical (scalar) apparent permeability is given by (Ghaddar 1995a,b)

$$k_h^a \equiv k_{h,11}^a = \frac{1}{T|Q_h|Re'}\int_0^T \int_{Q_h} K_{11}^h \, \mathrm{d}\mathbf{y}\, \mathrm{d}t, \tag{50}$$

or, alternatively,

$$k_h^a = \frac{1}{T|Q_h|Re'}\{U^i\}^T[A]\{U^i\} = \frac{1}{T|Q_h|Re'}\{1\}^T[M]\{U^1\}. \tag{51}$$

For steady-state flows, no averaging in time is needed, and 50–51 reduce, respectively, to

$$k_h^a = \frac{1}{|Q_h| Re'} \int_{Q_h} K_{11}^h \, \mathbf{dy}, \tag{52}$$

$$k_h^a = \frac{1}{|Q_h| Re'} \{U^i\}^T [A] \{U^i\} = \frac{1}{|Q_h| Re'} \{1\}^T [M] \{U^1\}. \tag{53}$$

4 Geometrical Configurations for the Microstructures

As mentioned in Sect. 2, the geometry and distribution of the solid and fluid phases in the 3-D periodic cell Q defines entirely the microstructure of the porous medium of interest. In this study, four geometrical configurations for Q are employed: (i) the simple cubic array of spheres, (ii) the square array of infinitely long cylinders, (iii) the cubic lattices of cylinders introduced by Higdon and Ford (1996), and (iv) a configuration for the dendritic region of a solidifying alloy.

It is befitting to note that the computational approach laid out in this study is not restricted to any specific microgeometry configuration. Indeed, the present approach can be applied to any microstructure, idealized or real, simple or complex, whose geometrical domain may be adequately meshed by finite elements. Non-intrusive imaging methods exist, for example, reconstruction techniques and X-ray tomography (Torquato 2002), which permit to characterize the microstructure of an actual porous medium. Faessel et al. (2005) and Maire et al. (2007) have used X-ray tomography to reveal the complex microstructures of random cellulosic fibrous networks and cellular ceramics materials, respectively. Faessel et al. (2005) were able to apply finite elements successfully, to study the thermal conductivity behavior of the fibrous networks. Also, one may speculate that some, though not all, microstructures shown by Maire et al. (2007) can be dealt with computationally. One expects, however, that there will be porous microstructures, which are not (yet) amenable to finite-element treatment; such is frequently the case with natural systems (e.g., Neethirajan et al. 2006; Torquato 2002).

4.1 Simple Cubic Array of Spheres

The geometry of Q is composed of a sphere of unitary diameter placed at the center of a cube of edge $\lambda = (\pi/6\phi)^{1/3}$. The solid phase is represented by the sphere, and its volume fraction is ϕ. This configuration is used here for validation purposes only, against the creeping-flow results of Zick and Homsy (1982).

4.2 Square Array of Cylinders

The cell geometry is composed of a circle of unitary diameter placed at the center of a square of side $\lambda = (\pi/4\phi)^{1/2}$; the solid phase is represented by the circle. This is in fact a 2-D configuration, reproduced by the 3-D cell Q by placing a circular cylinder of unitary diameter (the solid fiber) at the center of a $\lambda \times \lambda \times \kappa\lambda$ parallelepipedal box. The factor κ is chosen to save CPU time, while avoiding meshing problems; typically $\kappa = 0.1$. The cylinder's axis is perpendicular to the pair of $\lambda \times \lambda$ faces. This configuration is used here for validation purposes also, against the inertial-flow numerical results of Ghaddar (1995a,b) for flow perpendicular to the cylinders.

4.3 Cubic Lattice Configurations

Three cubic lattice arrays are presented, in detail, by Higdon and Ford (1996), denoted by simple cubic (SC), body-centered cubic (BCC), and face-centered cubic (FCC); it should be noted that these denominations, and respective acronyms, are used in the literature to refer to both arrays of cylinders and arrays of spheres (Kaviany 1995). The fibers are straight circular cylinders that intersect at the points corresponding to the nodes of the arrays. Higdon and Ford (1996) present numerical results for the permeability of such arrays with no consideration to inertial effects. While these permeability results will also be compared to the present results, the main motivation for considering this geometrical configuration is the ability to quantify the inertial effects in such media. Thus, some new results for the apparent permeability of the cubic lattice arrays are presented for several Reynolds numbers.

It is important to note that useful physical information is obtained, when analyzing transport phenomena in idealized ordered microstructures. First, different ordered microstructures are found in several engineering applications, including fluid flow and heat transfer (Bear 1988; Kaviany 1995; Higdon and Ford 1996; Tian et al. 2004). Second, the structural parameters and packing characteristics (Kaviany 1995) of the SC, BCC, and FCC arrays are dissimilar. Thus, for the same porosity, the arrays will present distinct pathways for fluid flow (and heat transfer), leading to different permeability and apparent permeability (and effective conductivity) values. Third, ordered microstructure configurations are relatively more amenable to experimental reproduction, such that they serve for validation of analytical and numerical models. One then establishes, that it is physically meaningful to consider the inertial effects and apparent permeability values associated with small to moderate Reynolds number flows in such microstructures. However, there are other physical scenarios, for which the SC, BCC, and FCC configurations are not suitable. As a relevant example, described in the next paragraph, the branching-like structures formed in the solidification of metal alloys are inherently different from the ordered arrays considered, so far. Therefore, the knowledge of the macroscopic flow characteristics in these branching structures is a key to warrant the ultimate quality of the alloy.

4.4 Dendritic Configuration

The solidification of alloys is a typical multiscale phenomenon, and the knowledge of both micro and macroscopic effects must be integrated to improve casting design (Stoehr 1998). During the solidification process of metal alloys, a finite two-phase mixture region may form between the solid and liquid phases, called the mushy region or mushy zone (Kaviany 1995; Prescott et al. 1991). The mushy zone is a porous material, where solid three-dimensional dendritic-like shapes form, grow, and fatten through the permeating interdendritic liquid. It is well-known that the flow of the liquid phase through the dendrites is responsible for many types of macrosegregation, so that, the permeability of the mushy zone is a key parameter for the final microstructure of the alloy (Poirier 1987; Heinrich et al. 1996). Since the permeability depends strongly on the microstructure of the medium, an adequate three-dimensional representation of dendrite morphology is thus a natural pursuit (McCarthy 1994). Additionally, although flow through the interdendritic region is, in general, considered to be Stokesian (Murakami et al. 1984; Poirier 1987), there exist situations for which inertial effects cannot be neglected (Nagelhout et al. 1995; Bousquet-Melou et al. 2002).

Dendrites may assume several different shapes in the mushy zone; the shape with cruciform cross-section appears to be the most relevant. In this type of microstructure, primary dendrite arms grow from the solid–liquid interface toward the liquid phase. Secondary dendrite arms grow from the primary ones, forming cruciform structures, when a section perpendicular to the primary arms is observed. It is remarked that, as the base of the primary dendrite is fixed to the solid–liquid interface, the entire dendritic structure is immobile and invariant under the action of the flow. In this study, specifically, it is attempted to represent the microstructure shown in the micrograph of Fig. 7 of Murakami et al. (1983), where both transverse and longitudinal sections of a translucent borneol–paraffin binary alloy sample are depicted. The goal is, therefore, to create a basic geometrical configuration for simulating the samples of Murakami et al. 1984, by matching approximately numerical results with the experimental values for the permeability, presented for flow parallel to the primary dendrite arms (the alloy type, and perhaps even some samples, seem to be the same for both studies of Murakami et al. (1983, 1984)).

Murakami et al. (1984) consider 32 experimental cases. Clearly, no unique configuration will be able to reproduce all cases (Rocha 2007). The best geometric solution rendered here is able to contemplate 17 experimental cases, leading to reasonably good approximations to the experimental parallel-flow permeability values, for the respective solid volume fractions (Sect. 5.3.1). When analyzing Fig. 7 of Murakami et al. (1983), one infers that, with respect to flow parallel to the primary dendrite arms, the disk-like shapes that appear at the end of each secondary dendrite arm are the main constituent elements of the microstructure. Therefore, their size and distribution over the space are the main factors that should be accounted for, when tailoring a geometrical configuration for the periodic cell, that ought to be suited for flow simulation and permeability calculation.

A simple geometrical configuration is then conceived (Rocha 2007), where the solid phase is composed of one entire cylinder plus four quarters of a cylinder, as shown in Fig. 1. As the cell is periodic in all three directions, one can realize that the entire constructed medium is formed by a three-dimensional ordered array of small cylinders, which represent the disk-like shapes cited above. These cylinders are disposed in a staggered way, so that preferential flow paths are minimized. Other tentative configurations (Rocha 2007) that did not avoid preferential flow paths, had permeability values much higher than the experimental ones. The dimension λ_1 is the distance between primary dendrite arms, λ_2 is the distance between secondary dendrite arms, d is the cylinder diameter, and c is the thickness of the secondary dendrite arm (height of the cylinders). In Fig. 7 of Murakami et al. (1983), one identifies that the thickness of the disk-like shapes is approximately 0.7 times the secondary dendrite arm spacing. Thus, the ratio $r = c/\lambda_2 = 0.7$ is imposed in the geometrical configuration for all cases, except when appropriate cell construction and meshing require the values $r = 0.75$ or $r = 0.8$. The diameter d is then calculated from $d = \lambda_1\sqrt{\phi/(r\pi)}$. In order to wrap up, given the experimental values (λ_1, λ_2, and ϕ), the periodic cell depicted in Fig. 1 can be constructed, and, therefore, associated permeability values can be calculated.

5 Results and Discussion

The objectives of this section are: (i) to validate the implementations for both creeping and inertial flows, against results available in the literature, (ii) to obtain new results for inertial flow in the cubic lattice arrays of cylinders of Higdon and Ford (1996), (iii) to compare numerical results for (Stokes) permeability of dendritic microstructures with the experimental ones obtained by Murakami et al. (1984) for flows parallel to the primary dendrite arms, (iv) to quantify inertial effects for the latter flows and, (v) to analyze the behavior of the numerical apparent permeability in the light of existing macroscopic laws. It must be remarked that the

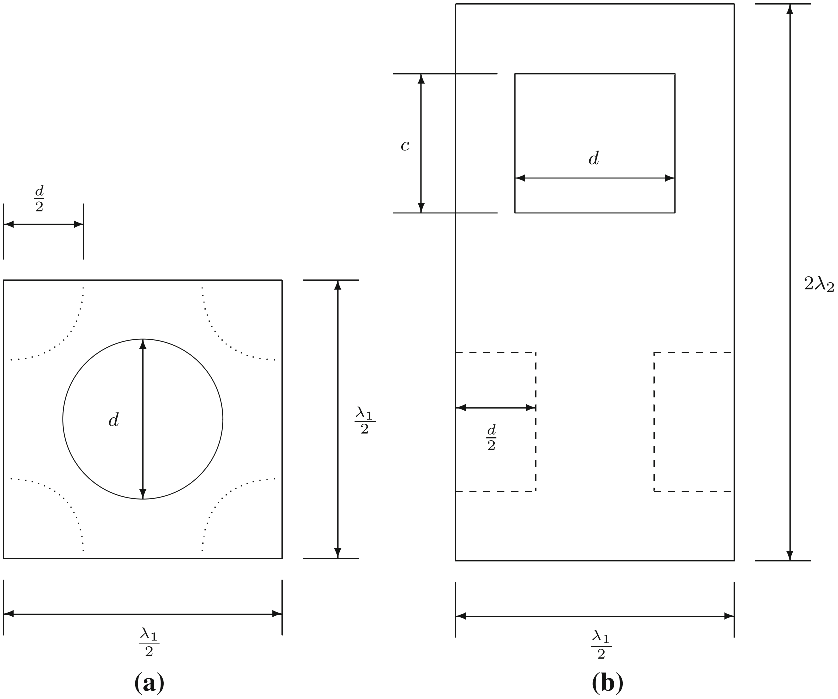

Fig. 1 Periodic cell geometry for the dendritic microstructure: **a** cross-section, and **b** longitudinal section. The solid phase (i.e., the cylinder and four quarters of a cylinder) is immobile and invariant under the action of the flow

calculated permeability k_h and apparent permeability k_h^a are normalized with respect to the diameter d.

5.1 Validation

5.1.1 Creeping Flow

Validation for creeping flow is effected for four different geometries of the periodic cell: (i) simple cubic array of spheres, (ii) simple cubic array of cylinders, (iii) body-centered cubic array of cylinders, and (iv) face-centered cubic array of cylinders.

For flow through a simple cubic array of spheres, numerical permeability results are compared to those of Zick and Homsy (1982). Actually, the results of Zick and Homsy (1982) are in the form of a ϕ-dependent drag coefficient $f = F/(3\pi\mu dq)$, where F is the (dimensional) mean drag force exerted by the fluid on each sphere, q is the superficial velocity of the flow, and d is the sphere diameter. The drag coefficient f can be related to the non-dimensional scalar permeability k by combining the momentum balance for the fluid with Darcy's law, leading to $k = 1/(18\phi f)$. In Table 1, it is possible to observe the very good agreement obtained between the present numerical results for the permeability k_h and the results of Zick and Homsy (1982) k_{ZH} for different values of the solid volume fraction ϕ.

For the simple (SC), body-centered (BCC), and face-centered (FCC) cubic arrays of cylinders, Higdon and Ford (1996) calculate the permeability numerically using the spectral

Table 1 Permeability results for creeping flow through the simple cubic array of spheres, for different values of the solid volume fraction ϕ

ϕ	k_h	k_{ZH}	δk (%)
0.125	0.1036	0.1036	0
0.216	0.03457	0.03456	0.03
0.343	0.01052	0.01052	0
0.450	0.004398	0.004394	0.09

Symbols k_h and k_{ZH} denote the permeabilities calculated in this study and by Zick and Homsy (1982), respectively; δk denotes the relative deviation of k_h with respect to k_{ZH}

Table 2 Permeability results for creeping flow through the simple cubic (SC), body-centered cubic (BCC), and face-centered cubic (FCC) arrays of cylinders, for different values of the solid volume fraction ϕ

SC				BCC				FCC			
ϕ	k_h	k_{HF}	δk (%)	ϕ	k_h	k_{HF}	δk (%)	ϕ	k_h	k_{HF}	δk (%)
0.228	0.1066	0.1066	0	0.557	0.006695	0.006680	0.22	0.235	0.1005	0.1010	0.50
0.348	0.03438	0.03430	0.23	–	–	–	–	0.379	0.02514	0.02528	0.55
0.412	0.01960	0.01955	0.26	–	–	–	–	–	–	–	–
0.543	0.006026	0.006035	0.15	–	–	–	–	–	–	–	–

Symbols k_h and k_{HF} denote the permeabilities calculated in this work and by Higdon and Ford (1996), respectively; δk denotes the relative deviation of k_h with respect to k_{HF}

boundary element method; only the Stokes regime is studied. In Table 2, the present numerical results for the permeability k_h of the SC, BCC, and FCC arrays are seen to agree very well with the results of Higdon and Ford (1996) k_{HF} for different values of ϕ. Note that, here, k_{HF} is non-dimensionalized with respect to the diameter, such that it is obtained by dividing the original results by 4.

5.1.2 Inertial Flow

There seem to be no analytical (exact) solutions for the apparent permeability for moderate Reynolds number flows, even in the case of simple ordered geometries. Ghaddar (1995a,b) uses finite elements to compute the apparent permeability for two-dimensional arrays of infinitely long cylinders, while Koch and Ladd (1997) employ a lattice-Boltzmann technique to compute the non-dimensional mean drag per unit length for such arrays. The non-dimensional drag coefficient of Koch and Ladd (1997) is given by $f = F/(\mu q)$, where F is the dimensional mean drag force per unit length. Again, by combining the momentum balance with Darcy's law, it can be derived that $k^a = \pi/(4\phi f)$. In order to validate the implementation for inertial flows against the results of Ghaddar (1995a,b) and Koch and Ladd (1997), three-dimensional calculations are performed in the ordered cell configuration, where the cylinder touches a pair of opposing faces, so that the two-dimensional geometry is simulated.

In Table 3, two sets of data are presented. In the first set, the present numerical results for the apparent permeability k_h^a are shown together with those by Ghaddar (1995a,b) k_{G}^a and by Koch and Ladd (1997) k_{KL}^a (originally in graphical form) for $\phi = 0.2$ and for different values of the *physical* Reynolds number $Re = \rho q d/\mu$ based on the superficial velocity q.

Table 3 Apparent permeability results for inertial flow through the square array of cylinders, for different values of the solid volume fraction ϕ and Reynolds number Re

$\phi = 0.2$							$\phi = 0.3$				
Re'	k_h^a	k_{G}^a	δk^a (%)	k_{KL}^a	δk^a (%)	Re	Re'	k_h^a	k_{G}^a	δk^a (%)	Re
17.2	0.06675	0.06602	1.1	0.068	1.8	19.5	29.9	0.02251	0.02221	1.4	19.9
25.2	0.06231	0.06141	1.5	0.063	1.1	40.0	44.2	0.02078	0.02042	1.8	39.9
30.0	0.06044	0.06055	0.18	0.061	0.92	54.5					

Symbols k_h^a, k_{G}^a, and k_{KL}^a denote the apparent permeabilities calculated in this study, by Ghaddar (1995a,b), and by Koch and Ladd (1997), respectively; δk^a denotes the relative deviation of k_h^a with respect to k_{G}^a or k_{KL}^a

The Re number cannot be prescribed *a priori*, but it can be calculated *a posteriori* in terms of the input parameter Re', through the expression (Ghaddar 1995b; Rocha 2007)

$$Re = k_h^a\,(Re')^2. \tag{54}$$

The values of Re, in Table 3, are the ones obtained by Ghaddar (1995a). In the second set of data, results are shown for $\phi = 0.3$ and different values of Re'; Koch and Ladd (1997) do not present results for the square array for any solid volume fraction other than 0.2.

Table 3 shows that the present results, k_h^a, are in good agreement with the ones by Ghaddar (1995a), k_{G}^a; the maximum discrepancy between them is lower than 2%. In particular, for $\phi = 0.2$, good agreement is also verified when k_h^a is compared to k_{KL}^a. For a given solid volume fraction ϕ, one observes that the higher the Reynolds number, the lower is the apparent permeability. This behavior means, physically, that the resistance to flow increases when more inertia is present in the flow.

5.2 Cubic Arrays of Cylinders

In this section, some new apparent permeability results for inertial flow through the three-dimensional cubic arrays of cylinders detailed in the study of Higdon and Ford (1996) are presented. In Table 4, the numerical results, k_h^a, are shown for the SC, BCC, and FCC arrays of cylinders, for different solid volume fractions ϕ and Reynolds numbers Re. The results for $Re = 0$, already shown in Table 2, are repeated for convenience. As expected, for a given array type and solid volume fraction, the apparent permeability decreases as the Reynolds number increases, due to increased resistance as the flow is more inertial. Also, the apparent permeability decreases as the solid volume fraction increases. This is due to increased resistance in the narrower paths for fluid flow at higher values of ϕ.

5.3 Dendritic Microstructure

5.3.1 Comparison with Experimental Results

Murakami et al. (1984) present experimental results for creeping flow through dendritic microstructures in borneol–paraffin binary alloy samples, the flow being parallel to the primary dendrite arms; the authors assert that inertial effects are negligible in their experiments. Using the creeping-flow formulation of Sect. 3.2.1, together with the geometrical configuration, depicted in Sect. 4, for the periodic cell, numerical results for k_h are obtained, shown in Table 5. Also shown in Table 5 are the experimental results of Murakami et al. (1984)

Table 4 Apparent permeability results for inertial flow through the simple cubic (SC), body-centered cubic (BCC), and face-centered cubic (FCC) arrays of cylinders, for different values of the solid volume fraction ϕ and Reynolds number Re

SC array			BCC array			FCC array		
ϕ	Re	k_h^a	ϕ	Re	k_h^a	ϕ	Re	k_h^a
	0	0.1066		0	0.006695		0	0.1005
0.228	8.7	0.0903		0.7	0.00668	0.235	4.2	0.0858
	9.7	0.0893	0.557	2.6	0.00655		7.4	0.0736
	0	0.03438		5.7	0.00634		0	0.02514
0.348	3.2	0.0323		9.8	0.00613	0.379	2.4	0.0241
	11.3	0.0283	–	–	–		8.0	0.0201
	0	0.01960	–	–	–	–	–	–
0.412	1.9	0.0191	–	–	-	–	–	–
	6.8	0.0170	–	–	–	–	–	–
	0	0.006026	–	–	–	–	–	–
0.543	4.8	0.00537	–	–	–	–	–	–
	11.9	0.00475	–	–	–	–	–	–

Symbol k_h^a denotes the apparent permeability calculated in this study

Table 5 Dimensional numerical permeability results k_h for creeping flow through the dendritic microstructure of Fig. 1, for different values of the solid volume fraction ϕ

case	serie	ϕ	$k_{\mathrm{M}}(\mu\mathrm{m}^2)$	$k_h(\mu\mathrm{m}^2)$	$k_{\mathrm{DT}}(\mu\mathrm{m}^2)$
2	A	0.566	10.4	14.5	844
6	A	0.502	15.2	29.1	1230
7	B	0.475	13.3	21.5	838
9	B	0.504	12.9	17.7	708
13	B	0.500	11.1	18.2	724
16	B	0.573	10.1	8.64	470
17	B	0.573	8.98	8.64	470
18	B	0.482	17.8	30.3	805
19	B	0.482	20.4	30.3	805
20	B	0.500	17.1	18.2	724
21	B	0.514	21.0	16.6	667
22	B	0.517	19.7	15.0	656
23	C	0.476	30.7	18.6	1440
25	C	0.504	22.1	15.3	1220
27	C	0.483	27.9	17.7	1380
29	C	0.578	17.8	6.49	785
32	C	0.394	62.3	36.4	2310

Symbols k_{M} and k_{DT} denote the permeabilities measured by Murakami et al. (1984) in the experiments indicated by "serie" and "case", and calculated by Drummond and Tahir (1984) for fluid flow parallel to a square array of infinite cylinders, respectively.

k_{M} for each triplet $(\lambda_1, \lambda_2, \phi)$. The "serie" indication in the table refers to the pair (λ_1, λ_2): series A, B, and C are used to designate (λ_1, λ_2) equal to $(420,\ 115)\,\mu\text{m}$, $(320,\ 90)\,\mu\text{m}$, and $(420,\ 90)\,\mu\text{m}$, respectively. The "case" indication refers to the experimental case label given by Murakami et al. (1984); as already mentioned in Sect. 4, only 17 of the 32 original cases are considered. For reference purposes, in Table 5, are also displayed the permeability results of Drummond and Tahir (1984) for fluid flow parallel to a square array of infinite cylinders k_{DT} with the corresponding volume fraction ϕ.

From Table 5, one may decide that the geometrical configuration developed is indeed appropriate for simulating the dendritic microstructure, since (i) the results obtained with the configuration is in reasonable agreement with the experimental values (in fact, much closer than the results obtained with the simpler model of Drummond and Tahir (1984) for fibrous media k_{DT}), and (ii) the proposed geometrical configuration includes the main components of the real dendritic microstructure of Murakami et al. (1984).

5.3.2 Evaluation of Inertial Effects

Based on the numerical prediction of the Stokes permeability for the dendritic microstructure, the inertial effects are now quantified through the calculation of the apparent permeability. According to Nagelhout et al. (1995), inertial effects are relevant in the mushy zone, when the solid volume fractions are smaller than 0.3. In fact, the solid volume fraction in the mushy zone is not constant in space, varying from 0 to 1 as the liquid or solid phase is approached, respectively. Thus, one can infer that, although Murakami et al. (1984) have studied portions of the mushy zone with $\phi > 0.3$, there probably exist other portions of the same mushy zone that have $\phi < 0.3$, where inertial effects should not have been negligible. Hence, using the same geometrical configuration, described in Sect. 4, for the dendritic microstructure, a periodic cell is built with $\phi = 0.250$, $\lambda_1 = 420\,\mu\text{m}$, $\lambda_2 = 90\,\mu\text{m}$, and $r = 0.7$, so as to represent those portions of the mushy zone where inertial effects may be relevant.

In order to determine the appropriate range of Reynolds numbers to be considered, typical values for the velocity (v) and kinematic viscosity (ν) must be evaluated for mushy zone applications. From Bousquet-Melou et al. (2002) and references therein, $1 < v < 10$ mm/s, typically. Considering metallic alloys solidification, a suitable value for ν is that of mercury, $\nu \approx 1.0 \times 10^{-7}\,\text{m}^2/\text{s}$ (The Engineering ToolBox 2008). The characteristic length is the diameter of the cylinder, which is calculated as $d = \lambda_1\sqrt{\phi/r\pi} \approx 142\,\mu\text{m}$. Therefore, it is easy to conclude that the appropriate range of Reynolds numbers is $1.4 < Re < 14$, approximately. Some Reynolds numbers within this range are thus selected, and the corresponding results obtained for the nondimensional permeability and apparent permeability are plotted in the graph of Fig. 2. As expected, the apparent permeability decreases as the Reynolds number increases. In the range $0 < Re < 14.7$, k_h^a decreases by 7%, i.e., when neglecting inertial effects for the triplet $(\lambda_1, \lambda_2, \phi)$ considered, one may overestimate k by approximately 7%. Indeed, this value can be even higher for other triplets $(\lambda_1, \lambda_2, \phi)$, specially for smaller values of ϕ.

5.4 Comparison of Numerical Results with Existing Macroscopic 'Laws'

In this section, the apparent permeability results of Sects. 5.2 and 5.3 for inertial flows through the cubic arrays of cylinders and the dendritic microstructure, respectively, are analyzed in the light of existing porous media macroscopic seepage laws, namely, the Forchheimer law and the cubic law (Firdaouss et al. 1997; Skjetne and Auriault 1999; Chen et al. 2001; Fourar et al. 2004; Lucas et al. 2007). It is worthwhile to remark that, in the literature, one may use the

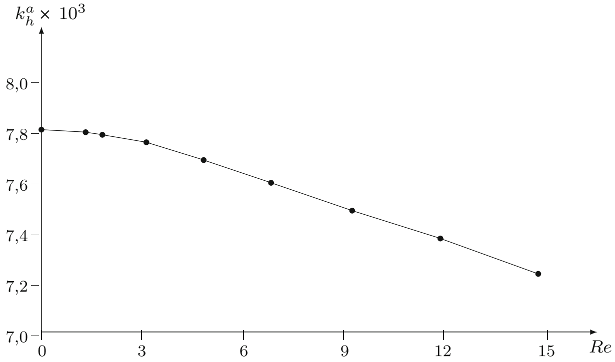

Fig. 2 Results for the numerical permeability and apparent permeability for flow through the dendritic microstructure of Fig. 1, for different Reynolds numbers Re. The solid volume fraction is $\phi = 0.250$, and the geometrical parameters are $\lambda_1 = 420\,\mu$m, $\lambda_2 = 90\,\mu$m, and $r = c/\lambda_2 = 0.7$

expression 'cubic law' when referring to parallel-plate-flow permeability of fractured media (e.g. in geophysical studies, Sisavath et al. 2003), or when referring to a cubic correction to Darcy's law; here, the expression is used in the latter sense.

In order to simplify the presentation, for a one-directional steady flow through a porous medium in the absence of gravity, Darcy's law is first written algebraically as

$$-\frac{\Delta P}{L} = \frac{\mu}{k^*} q\,, \tag{55}$$

where ΔP is the pressure drop across the medium macroscale L, through which a Newtonian fluid with constant viscosity μ (and density ρ) flows with seepage velocity q; k^* is the medium dimensional permeability. Based on Eq. 55, the Forchheimer law may then be written as

$$-\frac{\Delta P}{L} = \frac{\mu}{k^*} q + \beta^* \rho q^2\,, \tag{56}$$

where β^* (in m^{-1}) is the ('rock-dependent') inertial resistance coefficient. For the ranges of Reynolds number investigated here, the modified Forchheimer equation with a Forchheimer's permeability (Skjetne and Auriault 1999; Fourar et al. 2004) is not considered. The cubic law, in turn, may be expressed as

$$-\frac{\Delta P}{L} = \frac{\mu}{k^*} q + \frac{\gamma' \rho^2}{\mu} q^3\,, \tag{57}$$

where γ' is a non-dimensional ('rock-dependent') weak inertia coefficient. Following Lucas et al. (2007) (an equivalent formulation is presented by Firdaouss et al. 1997), a velocity-dependent apparent permeability may be defined as

$$k^{a*} = \frac{\mu}{-(\Delta P/L)} q\,, \tag{58}$$

such that Eqs. 56 and 57 can be rewritten, respectively, as

$$\frac{1}{k^{a*}} = \frac{1}{k^*} + \frac{\beta^* \rho}{\mu} q\,, \tag{59}$$

$$\frac{1}{k^{a*}} = \frac{1}{k^*} + \frac{\gamma' \rho^2}{\mu^2} q^2\,. \tag{60}$$

Finally, Eqs. 59 and 60 can be made nondimensional by choosing the cell size l as the microscopic length scale and q as the velocity scale, such that after some manipulation those equations, respectively, become

$$\ln\left(\frac{1}{k^a} - \frac{1}{k}\right) = \ln(Re) + \ln(\beta)\ , \tag{61}$$

$$\ln\left(\frac{1}{k^a} - \frac{1}{k}\right) = 2\ln(Re) + \ln(\gamma)\ , \tag{62}$$

where $k^a = k^{a*}/l^2$ and $k = k^*/l^2$ are the nondimensional permeabilities, $Re = \rho q d/\mu$ is the microscopic Reynolds number, d is the characteristic grain size, and $\beta = \beta^*(l^2/d)$, $\gamma = \gamma'(l^2/d^2)$. Clearly, from Eqs. 61 and 62, when one displays the difference $(1/k^a - 1/k)$ against the Reynolds number on a log–log plot (the so-called Forchheimer plot), a straight line with slope 1 results when Forchheimer law applies, whereas a straight line with slope 2 results when the cubic law applies.

For 2-D and 3-D unbounded periodic porous media, which satisfy the flow reversibility condition (termed Hypothesis H), Firdaouss et al. (1997) demonstrate, mathematically, that there are two zones of dependence of the pressure gradient with respect to the seepage velocity: in the asymptotic Darcy zone, as $Re \to 0$ (Re is the microscopic Reynolds number based on grain size), the first nonlinear correction term to Darcy's law is cubic with respect to the seepage velocity (or quadratic in terms of Re); in the second zone (high-Re flows), inertia dominates and the first correction term to Darcy's law is quadratic with respect to the seepage velocity (or linear in terms of Re). Therefore, according to the study of those authors, in the Darcy zone the cubic law applies, and as Re increases beyond this zone, Forchheimer law applies. It is noted that for 1-D flows in porous media or for homogeneous isotropic porous media, Mei and Auriault (1991) prove that the same two zones exist, just as long as the fluid is incompressible. In order to substantiate their analytical results, Firdaouss et al. (1997) reinspect classical filtration experimental results, and perform numerical calculations for 2-D steady-state Navier-Stokes flows. For the 2-D cells, which satisfy Hypothesis H, the calculations show that the Darcy zone extends up to $Re = O(10)$.

Skjetne and Auriault (1999) use the homogenization technique to model the nonlinearities in laminar flows through porous media, and show that the cubic weak-inertia regime is valid for any degree of anisotropy of the porous matrix, when $\epsilon^{1/2} \ll Re \ll 1$. They, thus, relax the flow reversibility condition of Firdaouss et al. (1997). Skjetne and Auriault (1999) further indicate the flow regimes for geometrically simple and geometrically complex porous media, however, they do not provide explicit definitions of these two classes of media. For geometrically simple media, the flow regimes are Darcy, weak inertia, strong inertia, and turbulence. For geometrically complex media, the flow regimes are Darcy, weak inertia, transition from weak to strong inertia (pore-geometry dependent), strong inertia, transition from strong inertia to turbulence, and turbulence. The authors also point out that a spline may be applied to the weak-to-strong inertia transition regime.

Fourar et al. (2004) refer to a controversy related to experimental and theoretical predictions, when inertial effects are present in single-phase laminar flows through porous media. They propose to explain the differences by investigating computationally, the influence of the flow dimension on the flow patterns and the behavior of the pressure and shear stress at the fluid/solid interface. Fourar et al. (2004), thus, perform 2-D and 3-D numerical simulations of steady-state flows through periodic porous media cells, respectively, with cylindrical and spherical inclusions. They compute the individual contributions of the form drag and viscous drag to the deviations from Darcy's law, and conclude that the total drag depends on the flow

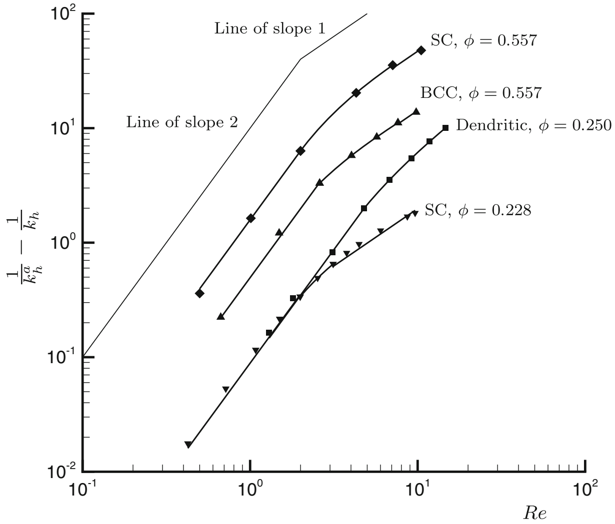

Fig. 3 Forchheimer plot, difference $(1/k_h^a - 1/k_h)$ versus microscopic Reynolds number $Re = \rho q d/\mu$, corresponding to calculated apparent permeability results for inertial flows through the SC cubic array of cylinders with solid volume fractions $\phi = 0.228$ and $\phi = 0.557$, the BCC array with $\phi = 0.557$, and the dendritic microstructure with $\phi = 0.250$

dimension. Consequently, for 3-D, Fourar et al. (2004) identify the following zones: Darcy for very low Re (roughly $Re < 2$, Reynolds number Re based on seepage velocity and grain size), transition or weak inertia (roughly $2 \leq Re < 4$, a very short zone in 3-D), and strong inertia (roughly $Re \geq 4$). In the latter zone, Forchheimer law applies.

Lucas et al. (2007) state that the physical explanation for the nonlinear deviation from Darcy's law is still an issue. Differently from the previous studies, they explore the influence of the flow periodicity or non-periodicity on the functional form of the macroscopic seepage law. Lucas et al. (2007) perform numerical simulations of high velocity flows through 2-D crenellated-channel porous media. Since their simulations are two-dimensional, and because Fourar et al. (2004) had proved the influence of the flow dimensionality upon the deviation from Darcy's law, the conclusions of Lucas et al. (2007) are not directly applicable to the present study.

In order to contribute to the (numerical) verification of the validity of the macroscopic porous media filtration laws, calculated apparent permeability results for inertial flows through the 3-D periodic microstructures of this study are now examined with the aid of Eqs. 61 and 62. Specifically, the functional behavior of the difference $(1/k_h^a - 1/k_h)$ with respect to the microscopic Reynolds number is analyzed, for the SC cubic array of cylinders with solid volume fractions $\phi = 0.228$ and $\phi = 0.557$, the BCC array with $\phi = 0.557$, and the dendritic microstructure with $\phi = 0.250$. The Forchheimer log–log plot is thus constructed, displayed in Fig. 3, by graphing $(1/k_h^a - 1/k_h)$ against Re. It is noted that, for the sake of this analysis, values of the Reynolds number up to $O(10)$ only have been considered; also, for the cubic arrays, more data points are plotted in Fig. 3 than entries are shown in Table 4.

From the analysis of Fig. 3 and the corresponding data, to within the numerical discretization errors, one may verify that all microstructures seem to fall in the class of geometrically complex media of Skjetne and Auriault (1999), in the sense that they induce the existence of three distinct laminar-flow zones of dependence of the difference $(1/k_h^a - 1/k_h)$ with

Table 6 Approximate ranges of validity for the cubic and Forchheimer laws, for the 3-D periodic SC cubic array of cylinders with solid volume fractions $\phi = 0.228$ and $\phi = 0.557$, the BCC array with $\phi = 0.557$, and the dendritic microstructure with $\phi = 0.250$

Configuration and solid Volume fraction ϕ	Weak inertia ($Re \to 0$) Cubic law	Weak-to-strong inertia transition	Strong inertia Forchheimer law
SC, $\phi = 0.228$	$Re < 2$	$2 \leq Re < 3.5$	$Re \geq 3.5$
SC, $\phi = 0.557$	$Re < 2$	$2 \leq Re < 7$	$Re \geq 7$
BCC, $\phi = 0.557$	$Re < 2.5$	$2.5 \leq Re < 7.5$	$Re \geq 7.5$
Dendritic, $\phi = 0.250$	$Re < 5$	$5 \leq Re$; upper limit not evaluated	–

respect to the Reynolds number Re. The first zone corresponds to very low Reynolds number flows, and is well-fitted by a straight line of slope 2. The third zone corresponds to the higher Reynolds number flows, and is well-fitted by a straight line of slope 1. The second zone is a transition from the first to the third zone, and is fitted by a spline. It is then verified numerically, that the cubic law is valid in the asymptotic ($Re \to 0$) weak-inertia zone, and that the Forchheimer law is valid in the strong-inertia zone. In Fig. 3, the dendritic microstructure displays the first two zones only, up to $Re = 15$. The approximate ranges of validity for each law may be estimated from the data, and are indicated in Table 6. Clearly, the range of validity for each law depends on the microstructure configuration and on the solid volume fraction. It appears that the range of validity is more sensitive to the nature of the microstructure than to the solid volume fraction. In agreement with the observation by Fourar et al. (2004), and given the 2-D results of Firdaouss et al. (1997), it is manifest that the range of validity for the cubic law is much shorter in 3-D than in 2-D. Finally, regarding the transition zone, its microstructure-dependent extent in 3-D is such that Forchheimer law begins ruling much sooner than in 2-D.

6 Conclusions

In this study, an analytical–numerical approach has been employed to predict numerical values for the permeability and apparent permeability of three-dimensional porous media, whose microstructures are given explicitly. The approach is based on the homogenization method for periodic structures, a control-volume type argument for inertial flows, and the finite-element method. Validation of the implementation, for both creeping and inertial flows, has been realized by comparison to results available in the literature.

Some new results for the apparent permeability of three-dimensional ordered arrays of cylinders have been obtained. The calculations indicate that, for a given array type and solid volume fraction, the apparent permeability decreases as the Reynolds number increases. Also, it decreases as the solid volume fraction increases. Physically, these trends are due to an increased flow resistance as the medium becomes less porous and the flow becomes more inertial, with more separated regions. Although expected qualitatively, the reported behavior of the apparent permeability has been here quantified accurately.

A rational, physically sound, and seemingly novel calculation route has been put forth to predict the apparent permeability of three-dimensional dendritic microstructures. First, a geometrical microstructural configuration is proposed, based on experimental observations of the solidification process of metal alloys. Second, the geometrical configuration is validated through comparison between experimental and numerical permeability results for the creeping-flow regime. Finally, inertial flows are considered for some typical Reynolds number values. Due to the inertial effects, the apparent permeability is again seen to decrease as the Reynolds number increases; quantitatively in the range investigated, it drops by a significant amount.

Perhaps most importantly, the rate of increase of an appropriate (numerical) difference function for the apparent permeability with respect to the microscopic Reynolds number is investigated via a Forchheimer plot. Several important facts are then numerically verified. First, the present 3-D microstructures are geometrically complex, and induce the appearance of three distinct laminar-flow zones of functional dependence: the asymptotic ($Re \to 0$) weak-inertia zone where the cubic law holds, the transition zone from weak inertia to strong inertia, and the strong inertia zone where the Forchheimer law holds. Second, the approximate ranges of validity for each law are indicated, and they depend on the solid volume fraction and, more strongly, on the microstructure configuration. Third, in view of available results in the literature, it is observed that the range of validity for the cubic law is much shorter in 3-D than in 2-D. Finally, the extent of the transition zone is microstructure-dependent, and is such that Forchheimer law begins ruling much sooner in 3-D than in 2-D.

In summary, this study successfully shows, through the utilization of complete continuous and discrete formulations for both creeping and inertial flows in three-dimensional porous media, and through permeability and apparent permeability quantitative evaluations, that oft-ignored inertial effects may, indeed, be relevant in many important engineering applications. Furthermore, for the 3-D periodic microstructures analyzed, the validity of existing porous media macroscopic seepage laws has been established. The analytical–numerical approach, due to its geometrical flexibility and its ability to predict the macroscopic flow properties of porous media with three-dimensional microstructures, thus presents itself as a valuable aid to experimental investigations.

Acknowledgements M.E. Cruz would like to thank the Brazilian Council for Development of Science and Technology (CNPq) for Grant PQ-306592/2006-1, and FAPERJ for Grant Cientista do Nosso Estado E-26/152.694/2006. The authors also thank Dr. Joachim Schöberl, from Johannes Kepler Universität Linz, Austria, for the free academic license of NETGEN 4.4. Finally, the authors are very grateful to the Reviewers for their many insightful comments.

References

Auriault, J.-L.: Homogénéisation. UJF, INPG, Grenoble, France (2001)

Bear, J.: Dynamics of Fluids in Porous Media. Dover Publications, Inc, New York (1988)

Bousquet-Melou, P., Goyeau, B., Quintard, M., Fichot, F., Gobin, D.: Average momentum equation for interdendritic flow in a solidifying columnar mushy zone. Int. J. Heat Mass Transf. **45**(17), 3651–3665 (2002)

Brown, S.G.R., Spittle, J.A., Jarvis, D.J., Walden-Bevan, R.: Numerical determination of liquid flow permeabilities for equiaxed dendritic structures. Acta Mater. **50**(6), 1559–1569 (2002)

Chen, Z., Lyons, S.L., Qin, G.: Derivation of the Forchheimer law via homogenization. Transp. Porous Media **44**(2), 325–335 (2001)

Drummond, J.E., Tahir, M.I.: Laminar viscous flow through regular arrays of parallel solid cylinders. Int. J. Multiph. Flow **10**(5), 515–540 (1984)

Edwards, D.A., Shapiro, M., Bar-Yoseph, Y., Shapira, M.: The influence of Reynolds number upon the apparent permeability of spatially periodic arrays of cylinders. Phys. Fluids A **2**(1), 45–55 (1990)

Faessel, M., Delisee, C., Bos, F., Castera, P.: 3D Modelling of random cellulosic fibrous networks based on X-ray tomography and image analysis. Compos. Sci. Technol. **65**(13), 1931–1940 (2005)

Firdaouss, M., Guermond, J.-L., Le Quere, P.: Nonlinear corrections to Darcy's law at low Reynolds numbers. J. Fluid Mech. **343**, 331–350 (1997)

Fourar, M., Radilla, G., Lenormand, R., Moyne, C.: On the non-linear behavior of a laminar single-phase flow through two and three-dimensional porous media. Adv. Water Res. **27**(6), 669–677 (2004)

Ghaddar, C.K.: Parallel analytico-computational methods for multicomponent media: application to thermal composites and porous-media flows. Ph.D. Thesis, Massachusetts Institute of Technology (1995a).

Ghaddar, C.K.: On the permeability of unidirectional fibrous media: a parallel computational approach. Phys. Fluids **7**(11), 2563–2586 (1995b)

Heinrich, J.C., Poirier, D.R., Nagelhout, D.F.: Mesh generation and flow calculations in highly contorted geometries. Comput. Methods Appl. Mech. Eng. **133**(1), 79–92 (1996)

Higdon, J.L.L., Ford, G.D.: Permeability of three-dimensional models of fibrous porous media. J. Fluid Mech. **308**, 341–361 (1996)

Hornung, U.: Homogenization and Porous Media. Springer-Verlag New York, Inc, New York (1997)

Kaviany, M.: Principles of Heat Transfer in Porous Media. 2nd edn. Springer-Verlag New York, Inc, New York (1995)

Lucas, Y., Panfilov, M., Bues, M.: High velocity flow through fractured and porous media: the role of flow non-periodicity. Eur. J. Mech. B/Fluids **26**(2), 295–303 (2007)

Koch, D.L., Ladd, A.J.C.: Moderate Reynolds number flows through periodic and random arrays of aligned cylinders. J. Fluid Mech. **349**, 31–66 (1997)

Maday, Y., Meiron, D., Patera, A.T., Rønquist, E.M.: Analysis of iterative methods for the steady and unsteady Stokes problem: application to spectral element discretizations. SIAM J. Sci. Comput. **14**(2), 310–337 (1993)

Maday, Y., Patera, A.T., Rønquist, E.M.: An operator-integration-factor splitting method for time-dependent problems: application to incompressible fluid flow. J. Sci. Comp. **5**(4), 263–292 (1990)

Maire, E., Colombo, P., Adrien, J., Babout, L., Biasetto, L.: Characterization of the morphology of cellular ceramics by 3D image processing of X-ray tomography. J. Eur. Ceram. Soc. **27**(4), 1973–1981 (2007)

Marušic-Paloka, E., Mikelic, A.: The derivation of a nonlinear filtration law including the inertia effects via homogenization. Nonlinear Anal. Theory Methods Appl. **42**(1), 97–137 (2000)

McCarthy, J.F.: Lattice gas cellular automata method for flow in the interdendritic region. Acta Metall. Mater. **42**(5), 1573–1581 (1994)

Mei, C.C., Auriault, J.-L.: The effect of weak inertia on flow through a porous medium. J. Fluid Mech. **222**, 647–663 (1991)

Murakami, K., Shiraishi, A., Okamoto, T.: Interdendritic fluid flow normal to primary dendrite-arms in cubic alloys. Acta Metall. **31**(9), 1417–1424 (1983)

Murakami, K., Shiraishi, A., Okamoto, T.: Fluid flow in interdendritic space in cubic alloys. Acta Metall. **32**(9), 1423–1428 (1984)

Nagelhout, D., Bhat, M.S., Heinrich, J.C., Poirier, D.R.: Permeability for flow normal to a sparse array of fibres. Mat. Sci. Eng. A-Struct. **191**(1), 203–208 (1995)

Neethirajan, S., Karunakaran, C., Jayas, D.S., White, N.D.G.: X-ray computed tomography image analysis to explain the airflow resistance differences in grain bulks. Biosyst. Eng. **94**(4), 545–555 (2006)

Ngo, N.D., Tamma, K.K.: Microscale permeability predictions of porous fibrous media. Int. J. Heat Mass Transf. **44**(16), 3135–3145 (2001)

Poirier, D.R.: Permeability for flow of interdendritic liquid in columnar-dendritic alloys. Metall. Trans. B **18**(1), 245–255 (1987)

Prescott, P.J., Incropera, F.P., Bennon, W.D.: Modeling of dendritic solidification systems: reassessment of the continuum momentum equation. Int. J. Heat Mass Transf. **34**(9), 2351–2359 (1991)

Reddy, J.N., Gartling, D.K.: The Finite Element Method in Heat Transfer and Fluid Dynamics. 2nd edn. CRC Press, Boca Raton, Florida (2001)

Rocha, R.P.A.: Permeability and apparent permeability of porous media with three-dimensional microstructures (in Portuguese). D.Sc. Thesis, COPPE/Federal University of Rio de Janeiro, Brazil (2007).

Schöberl, J.: NETGEN-4.0. Numerical and symbolic scientific computing, Johannes Kepler Universität Linz, Austria (2001).

Shewchuk, J.R.: An introduction to the conjugate gradient method without the agonizing pain. School of Computer Science, Carnegie Mellon University, Pittsburgh, Pennsylvania (1994).

Sisavath, S., Al-Yaarubi, A., Pain, C.C., Zimmerman, R.W.: A simple model for deviations from the cubic law for a fracture undergoing dilation or closure. Pure Appl. Geophys. **160**(5–6), 1009–1022 (2003)

Skjetne, E., Auriault, J.-L.: New insights on steady, non-linear flow in porous media. Eur. J. Mech. B/Fluids **18**(1), 131–145 (1999)

Stoehr, R.A.: Modeling the influence of fluid flow on the development of porosity and microstructure in castings. Can. Metall. Q. **37**(3-4), 179–184 (1998)

The Engineering ToolBox: Mercury Properties. http://www.engineeringtoolbox.com/mercury-d_1002.html (2008). Accessed 23 April 2008

Tian, J., Kim, T., Lu, T.J., Hodson, H.P., Queheillaltb, D.T., Sypeck, D.J., Wadley, H.N.G.: The effects of topology upon fluid-flow and heat-transfer within cellular copper structures. Int. J. Heat Mass Transf. **47**(14–16), 3171–3186 (2004)

Torquato, S.: Random Heterogeneous Materials, Microstructure and Macroscopic Properties. Springer-Verlag New York, Inc, New York (2002)

Zick, A.A., Homsy, G.M.: Stokes flow through periodic arrays of spheres. J. Fluid Mech. **115**, 13–26 (1982)